The Initial Composition of Jet Condensation Trails

B. Kärcher

Lehrstuhl für Bioklimatologie und Immissionsforschung, Universität München, Freising-Weihenstephan, Germany

Th. Peter and U. M. Biermann

MPI für Chemie, Mainz, Germany

U. Schumann

DLR Institut für Physik der Atmosphäre, Oberpfaffenhofen, Germany

ABSTRACT

Physicochemical processes that generate and transform aerosols in jet aircraft plumes are discussed on the basis of theoretical models and recent observations of young contrails in the upper troposphere. The initial evolution of optical depth and ice water content under threshold contrail formation conditions is studied. Constrained by the measurements, a lower bound is deduced for the number density of ice crystals initially present in contrails. This bound serves as a visibility criterion for young contrails. An analysis of the primary contrail particles (aqueous solution droplets nucleated in situ, emitted insoluble combustion aerosols, and entrained background aerosols) reveals that only soot must be involved as ice forming nuclei if the visibility criterion is to be fulfilled. Possible activation pathways of the soot aerosols are investigated, including an analysis of their wetting behavior and droplet scavenging and heterogeneous nucleation properties. To support these investigations, results of laboratory experiments concerning contact angles of acidic solution droplets on carbonaceous surfaces and the freezing probability of sulfuric acid tetrahydrate are presented. Assuming that the soot particles acquire a liquid coating, heterogeneous freezing rates and their sensitivity on important parameters are studied.

1. Introduction

Particulate emissions from jet aircraft operating in the upper troposphere and lower stratosphere can potentially increase the mass, particle number density, and chemical reactivity of the global background aerosol layer, thereby affecting both the chemical properties of the atmosphere and the radiative energy balance and hence global climate. The assessment of the possible influence of aircraft-induced aerosols on the atmosphere is an important element of the research programs currently carried out to address the issue of environmental effects of sub- and supersonic aviation (e.g., Schumann 1994; Stolarski and Wesoky 1995). In view of the sensitivity of upper-tropospheric aerosol properties and ice nucleation processes (Jensen and Toon 1994) and with regard to the importance of heterogeneous chemical reactions in the lower stratosphere, in particular their role in ozone depletion (e.g., Pyle et al. 1994), the injection of aerosol particles by

jet aircraft cruising at the tropopause level has become a significant research issue.

Experimental observations (Hofmann and Rosen 1978; Reiner and Arnold 1993; Baumgardner and Cooper 1994; Hagen et al. 1994) and theoretical investigations (Miake-Lye et al. 1994; Kärcher et al. 1995; Zhao and Turco 1995) strongly suggest that jet aircraft produce volatile sulfuric acid aerosols by homogeneous nucleation within the jet plume. Jet engines also inject carbonaceous particles (soot) into the atmosphere (e.g., Rosen and Greegor 1974; Pueschel et al. 1992; Hagen et al. 1992; Whitefield et al. 1993; Blake and Kato 1995). These two particle types constitute the major fraction of the primary aerosol that is modified due to condensation and coagulation among themselves and with the entrained aerosols when the plume cools and mixes with ambient air. Some of the primary aerosol particles may freeze if the ambient temperature is sufficiently low so that the plume becomes supersaturated with respect to ice during cooling. This results in the formation of the secondary aerosol containing both liquid and frozen volatile components and mixed particles, a fraction of which contains soot inclusions. On synoptic timescales these frequently observed ice condensation trails at tropopause flight levels interact with

Corresponding author address: Dr. Bernd Kärcher, Lehrstuhl für Bioklimatologie und Immissionforschung, Universität München, Hohenbachernstr. 22, D-85354 Freising-Weihenstephan, Germany.
E-mail: brk@atmosl.met.forst.uni-muenchen.de

the background aerosol. Upon evaporation, new cloud condensation nuclei and possibly also ice forming nuclei are released into the atmosphere. Depending on meteorological conditions and, thus, on their lifetimes these particles may trigger the formation of cirrus clouds and serve as sites for heterogeneous reactions. The interaction of the soot particles with H_2SO_4/H_2O droplets and trace gases in the jet plume may affect the surface properties of the carbon aerosols and their suitability to host heterogeneous chemical reactions. The interplay of these processes is shown schematically in Fig. 1. Up to now there are no models that comprehensively treat these possibly highly competitive microphysical and chemical processes in aging aircraft plumes (cf. Kärcher and Peter 1995). Unfortunately, very little information is available about the composition and nucleation properties of the carbonaceous particles under plume conditions.

In particular, it is presently unclear which particle type of the primary aerosol spectrum initiates ice crystal formation. Possible pathways are (a) activation and freezing of entrained ambient aerosol; (b) homogeneous freezing of the H_2SO_4/H_2O droplets; (c) heterogeneous freezing of the H_2SO_4/H_2O droplets on soot inclusions, which arise from heterogeneous nucleation or from droplet scavenging by the soot particles; (d) homogeneous or heterogeneous freezing of the solution droplets after uptake of additional solutes (e.g., HNO_3) or after heterogeneous chemical processing effectively leading to further solute uptake (e.g., heterogeneous SO_2 oxidation). Two other possible pathways, formation of ice crystals or pure water droplets via heterogeneous nucleation from the vapor phase, will be shown to be unlikely. Microphysical calculations suggest homogeneous nucleation, growth, and homogeneous freezing of H_2SO_4/H_2O droplets (pathway b) to be only effective when the plume during cooling becomes supersaturated with respect to water.

The primary objective of this work is to discuss some of the in situ transformation processes of the primary aerosol as summarized in Fig. 1 on the basis of two recent contrail observations in the upper troposphere (Busen and Schumann 1995; Schumann et al. 1996), supplemented by dynamical and microphysical simulations. The unique feature of these measurements was that contrails from a twin engine aircraft were observed with one of the engines operating on a jet fuel with very low, and the other with rather high sulfur contents. In detail, this paper focuses on a simple model describing the initial growth phase of ice particles immediately after freezing nucleation. We constrain the model by the observation that a visible contrail is formed typically within one wingspan behind the jet engine. We investigate how many (section 2) and which of the primary aerosol particles (section 3) most likely contribute to the ice mass budget of contrails. This investigation does not rely on details of the nucleation process itself, but it allows us to conclude that the soot aerosols
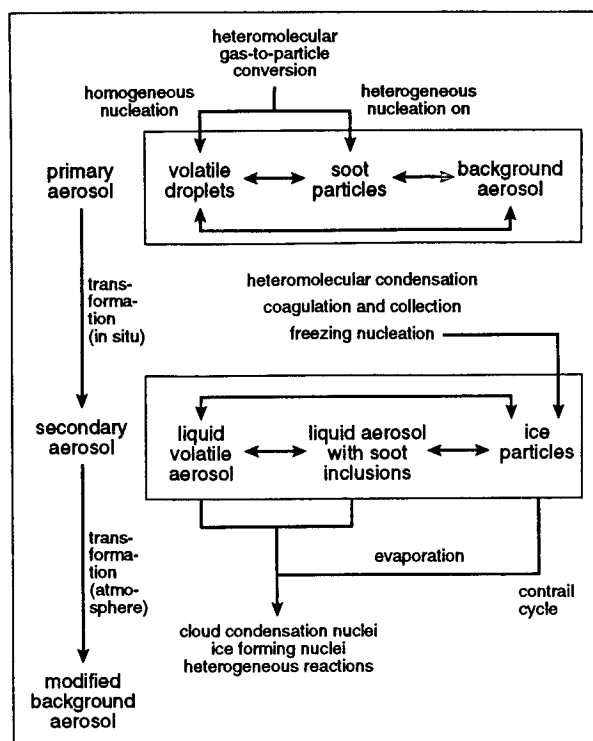

FIG. 1. Schematic illustration of the microphysical processes that generate and modify the types of aerosol particles in aging jet aircraft exhaust plumes. Key questions concern the production of new cloud condensation and ice forming nuclei and their possible influence on cloud formation and heterogeneous chemistry in the upper troposphere and lower stratosphere.

are very likely to participate in the contrail formation process in order to satisfy the visibility criterion. The great potential for chemical processing of the fresh soot particles in the very young aircraft plume, possibly through simultaneous action of several exhaust trace species like HNO_3, SO_2, and NO_2, may lead to favorable conditions for water adsorption and binary heterogeneous nucleation. Section 4 is devoted to the question of how the soot particles could acquire a liquid coating under plume conditions by studying the wetting behavior of black carbon aerosols and analyzing the gas phase budgets of various chemical trace species in the exhaust. These considerations are supported by laboratory experiments performed in order to measure the compatibility of carbonaceous surfaces with acidic solution droplets and to estimate the freezing probability of sulfuric acid tetrahydrate. The paper finishes with a discussion of nucleation rates for heterogeneous freezing, and the conclusions are given in section 5.

2. Initial contrail growth phase

This section briefly describes a contrail observation on which the microphysical investigations are based. We investigate the growth of ice particles in the early

jet plume just after freezing nucleation. A simple model, constrained by the observation that contrails always become visible within ~1 wingspan, allows us to find a lower bound for the number density of ice particles in young contrails.

a. Contrail observation

We refer to the contrail formation recently observed by Busen and Schumann (1995) under threshold conditions. Short-lived contrails were generated by the twin-engine jet aircraft ATTAS at $p_a = 302.3 \pm 0.7$ hPa, $T_a = 223.45 \pm 0.5$ K, and an ambient relative humidity around $RH_a = 34\%$. The humidity was estimated from nearby radiosoundings and could have been ~10% higher. The contrails became visible within 25–35 m behind the engines—that is, within 0.86–1.6 wingspans. Using a two-dimensional model describing the turbulent mixing of the jet with the ambient air (Kärcher et al. 1996), we compute the ice saturation profile behind the circular jet as a function of the axial distance past exit, x, and the radial direction perpendicular to the jet axis, y, by transporting the emitted water vapor as an inert tracer. The calculation was initialized with jet exit conditions derived from a mass, momentum, and energy budget analysis for this specific aircraft (Schumann et al. 1996). The result is shown in Fig. 2. At small x, the ambient ice saturation ratio is 0.54, corresponding to $RH_a = 34\%$, and humidity in the hot jet core and bypass (indicated by the step around $y = 0.2$ m) is negligible. With increasing values of x, the ice saturation ratio first increases in the mixing region, where the engine's water vapor is mixed into the relatively cold bypass. The mixing region moves radially away from the jet axis, leading to a distinct ridge in the saturation profile. The plume first becomes supersaturated with respect to ice at $x = 1.1$ m and $y = 0.48$ m at $T = 233$ K. Maximum values around 1.46 are first reached at $y \approx 1$ m at distances $x = 41$ m past exit. At later stages around $x = 130$ m (i.e., typically three times further away from the aircraft), such high values are also reached in the center of the jet. Contrail formation is initiated in the mixing region of the jet, several nozzle diameters behind the engine.

The calculation suggests that the plume was never supersaturated with respect to (liquid) water when the contrails were observed. During mixing of the hot and humid exhaust with ambient air, the plume reaches a maximum relative humidity of 97% (Schumann 1996), which we confirm by the present calculation. (Note that this is an upper bound because depletion of gaseous H_2O due to droplet or ice crystal growth is suppressed in the calculation.) We have also performed large eddy simulations of the coannular jet with H_2O treated as a passive scalar; they suggest that small patches of air might acquire relative humidities up to 107% in a short time window around 0.09 s because they penetrate the bypass without essential mixing. Due to the possible
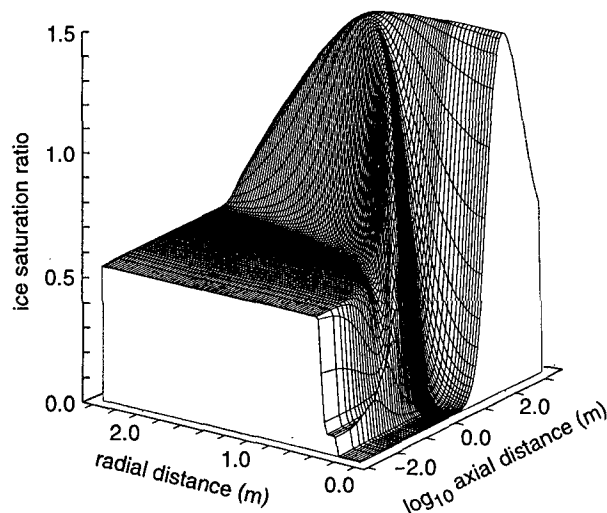

FIG. 2. Spatial distribution of the ice saturation ratio behind the ATTAS jet engine as a function of axial distance x and the jet radius y. The value $x = 0$ corresponds to the nozzle exit plane.

uncertainties in the fluid-dynamical simulation and in the determination of T_a and RH_a during the ATTAS contrail observation, we cannot exclude that the plume might have been slightly above water saturation. To investigate this possibility, we performed a calculation at lower air temperature, $T_a = 222.95$ K, and higher relative humidity, $RH_a = 45\%$, which are both within experimental uncertainties. In this case, the plume first becomes supersaturated with respect to water at $y = 0.72$ m off the jet axis at a distance $x = 58$ m behind the nozzle exit plane; the peak humidity is 105%. Clearly, this is much longer than the distance where the contrail was observed. Moreover, liquid droplets would grow slower than ice particles to become visible due to their greater saturation vapor pressure. Hence, we conclude that the contrail was very likely generated below the water saturation threshold.

b. Model description and input parameters

At the given flight altitude the ATTAS jet engine injects water vapor into the atmosphere with an emission index $EI_w = 1.215$ kg H_2O per kg fuel. This translates into an initial molecule number density $n_{w,i} = (EI_w/m_w)(\dot{f}/\dot{V}) = 9.7 \times 10^{16}$ cm^{-3}, where $m_w = 3 \times 10^{-23}$ g is the mass of an H_2O molecule, $\dot{f} = 0.126$ kg fuel s^{-1} is the engine's fuel flow rate, and $\dot{V} = 52.51$ m^3 s^{-1} is the volume increase of the jet at the nozzle exit plane. After a short cooling and dilution phase the plume becomes supersaturated with respect to ice. For the model we take this point as $t = 0$. The available water vapor is now $n_{w,0} = n_{w,i}\mathcal{D}_w$, where $\mathcal{D}_w = 4 \times 10^{-2}$ is the dilution factor for the ATTAS observation. (The resulting $n_{w,0} = 4 \times 10^{15}$ cm^{-3} is the water vapor abundance in the mixing region where supersaturation over

ice is first observed, see above.) At time $t' = 0$, we assume that monodisperse ice nuclei are present with number density n and radius r_0, onto which the available water vapor condenses. The growth of the ice crystals (which are assumed to be spherical) depletes the water vapor in the gas phase and increases the ice water content $m(t) = 4\pi \rho n r^3(t)/3$ of the particles, where ρ and $r(t)$ are the mass density of ice and the actual radius, respectively. We make the approximation that at $t = 0$ the temperature has already reached the ambient value $T_a = 223.45$ K and neglect the finite cooling time still necessary to cool from $T = 233$ K just at ice saturation to T_a. Together with the fact that we also ignore dilution of the ice particles due to ongoing entrainment, this implies that the timescales deduced below are lower bounds. Further, we assume that the ambient atmosphere is saturated with respect to ice, so that the growth stops when the transient supersaturation $s(t) = n_w(t)/n_{sat} - 1$ in the plume approaches zero. Here, n_{sat} denotes the number density of water molecules at ice saturation taken from Pruppacher and Klett (1978, 625), which under the ATTAS flight conditions is $n_{sat}(T_a) = 1.33 \times 10^{15}$ cm^{-3}. In reality the ATTAS contrails evaporated slowly because the ambient air was slightly subsaturated, but this does not affect our conclusions. In summary, the input parameters are given by $p_a = 302.3$ hPa, $T_a = 223.45$ K, and $s_0 = n_{w,0}/n_{sat}(T_a) - 1 = 2$. In the following, the evolution of the H$_2$O molecular number density in the gas phase, n_w, and the ice crystal radius, r, will be calculated, while the number density of ice crystals, n, and their initial radius, r_0, will be treated as free parameters.

c. Model equations and solution

The equations governing the evolution of the gas phase water vapor number density and the radius of the ice particles read

$$\frac{dn_w}{dt} = -j_w n, \qquad (1a)$$

$$\frac{dr}{dt} = \frac{j_w m_w}{4\pi \rho r^2}. \qquad (1b)$$

The flux of molecules to the ice particles is given by

$$j_w = 4\pi D r G_\alpha(r)[n_w - n_{sat}(T_a)], \qquad (2)$$

where $D(p_a, T_a)$ is the diffusivity of the vapor molecules in air and the function $G_\alpha(r)$ takes account of the transition of the uptake from the gas kinetic to the diffusional regime. This function is given by (Sedunov 1974, 24)

$$G_\alpha(r) = \left(\frac{1}{1 + \text{Kn}} + \frac{4\text{Kn}}{3\alpha} \right)^{-1}, \qquad (3)$$

with the deposition coefficient α, the Knudsen number $\text{Kn} = \lambda/r$, and the mean free path of the vapor mole-

cules in air, $\lambda(p_a, T_a)$. The function G_α takes the limiting values $G_\alpha \rightarrow 1$ for $\text{Kn} \rightarrow 0$ (diffusion limit) and $G_\alpha \rightarrow 3\alpha/(4\text{Kn})$ for $\text{Kn} \gg 1$ (free molecular regime). Values for the deposition of water molecules on ice between 0.014 and ~ 1 are referenced in Pruppacher and Klett (1978, p. 135), exhibiting a trend toward unity for low temperatures. In our calculation, we use $\alpha = 0.1$ and neglect the Kelvin barrier in (2) that enhances the saturation vapor density by $>10\%$ for particles with radii < 20 nm (and which implies only small changes compared to the range of uncertainty of α.) Corrections of the flux (2) due to heat conduction are likewise small and can therefore be neglected.

Upon elimination of j_w, (1a) and (1b) become $dr^3/dt \propto dn_w/dt$, from which a first integral of the differential equations is calculated. Introducing the ice supersaturation $s(t)$, this integral is

$$r^3 = r_{max}^3 - V_0 s, \qquad V_0 \equiv \frac{3m_w n_{sat}}{4\pi \rho n}. \qquad (4a)$$

The total mass balance then reads

$$r_{max}^3 = r_0^3 + V_0 s_0, \qquad (4b)$$

which defines the maximum radius of the ice particles at the end of the initial growth phase. The solution is most conveniently expressed in terms of the dimensionless variables $\tilde{r} = r/r_{max}$, $\tilde{s} = s/s_0$, and $\tilde{t} = t/t_0$, where t_0 is the characteristic time

$$t_0 = \frac{3}{4\pi D r_{max} n \alpha}. \qquad (5)$$

Equation (4a) then reads

$$\tilde{s}(\tilde{r}) = \kappa(1 - \tilde{r}^3), \qquad \kappa \equiv \frac{r_{max}^3}{V_0 s_0} \geqslant 1. \qquad (6a)$$

In these scaled quantities the second integral of (1a) and (1b) finally reads

$$\tilde{t}(\tilde{r}) = \int_{\tilde{r}_0(\kappa)}^{\tilde{r} \leqslant 1} \frac{\alpha \tilde{r}}{G_\alpha(\tilde{r}, \lambda/r_{max})(1 - \tilde{r}^3)} \, d\tilde{r}, \qquad (6b)$$

with the lower integration boundary defined by

$$\tilde{r}_0 \equiv \frac{r_0}{r_{max}} = \left(1 - \frac{1}{\kappa} \right)^{1/3}. \qquad (6c)$$

After solving the integral (6b) and inversion to obtain $\tilde{r}(\tilde{t})$, the supersaturation follows from (6a) and the ice water content $\tilde{m}$ (normalized by $4\pi r_{max}^3 \rho n/3$) may be computed from

$$\tilde{m}(\tilde{r}) = \tilde{r}^3 - \tilde{r}_0^3(\kappa). \qquad (6d)$$

Besides the weak dependence on λ/r_{max} these general solutions depend only on the dimensionless parameter $\tilde{r}_0$ and on α. The solutions are displayed in Fig. 3 for $\alpha = 0.5$ in the case $\tilde{r}_0 = 0$; the shaded region indicates the sensitivity of the growth when $\tilde{r}_0$ is varied between

0 and 0.15, and the horizontal bars show the scatter of $\tilde{r}(\tilde{t})$ when α is varied from 0.1 (left ends) to 1 (right ends). After an induction period lasting up to $\tilde{t} = 0.05$, radius and supersaturation start to depart from their initial values $\tilde{r}_0 = 0$ and $\tilde{s}_0 = 1$. Around $\tilde{t} = 0.2$, the quantities $\tilde{r}$, $\tilde{s}$, and $\tilde{m}$ rapidly change and take on their final values at times $\tilde{t} \approx 1$. The sensitivity with respect to α is small as long as the particles stay below $\tilde{r} < 0.2$, since in the free molecular regime $j_w \propto G_\alpha \propto \alpha$ and hence, the solution (6b) is independent of α. The sensitivity of the solutions with respect to variations of $\tilde{r}_0$ can be important, but only in the early growth stage. Note that the results for any particular problem can be easily read off the general solution in Fig. 3 after conversion to the scaled variables ($\tilde{r}, \tilde{t}, \tilde{s}, \tilde{m}$).

d. Visibility criterion

Figure 4 shows the evolution of the ice particle radius $r(t)$ and the ice water content $m(t)$ for $r_0 = 0.02$ μm and two different ice particle number densities $n = 10^3$ cm^{-3} and $n = 10^5$ cm^{-3}, using $\alpha = 0.1$. Clearly, particle growth reaches equilibrium earlier in the case of higher n because $t_0 \propto n^{-2/3}$ and the particles deplete the gas phase reservoir more rapidly. The final radius $r_{max} = 0.6$ μm is smaller in the case with $n = 10^5$ cm^{-3} than $r_{max} = 2.75$ μm for $n = 10^3$ cm^{-3}, because $r_{max} \propto n^{-1/3}$ and the same amount of vapor is distributed among more particles. The final ice water content $m_{max} = 8 \times 10^{-2}$ g m^{-3}, however, is identical in both cases [$n r_{max}^3 \approx$ const, see (4b)].

To explain the ATTAS observations we have to answer the basic question: How many ice crystals must

FIG. 4. Evolution of the ice particle radius r and the ice water content m as a function of time t after freezing for two different ice particle abundances n using $r_0 = 0.02$ μm and $\alpha = 0.1$. The final radii r_{max} scale as $r_{max} \propto n^{-1/3}$ and the typical growth timescales $\propto n^{-2/3}$.

be present initially in the plume in order to observe a visible contrail within 25–35 m? This may be translated into a time constraint for the solutions shown in Fig. 4 from which a lower bound for n may be derived: the ice crystals have to grow to a visible size within 0.2–0.3 s, using the true airspeed 115 m s^{-1} of the ATTAS aircraft. Next, the term "visibility" has to be quantified. Appleman (1953) estimates the visible water content of faint and distinct contrails in the range $m_v = 4 \times 10^{-3}$–10^{-2} g m^{-3}, respectively. The computation of the optical depth τ allows for a cross-check of this empirical visibility definition. It can be defined by

$$\tau(t) = \pi r^2(t) Q_{ext}(r) n l, \qquad (7)$$

with the extinction (essentially scattering) efficiency $0 \leqslant Q_{ext}(r) \leqslant 4$, which we take from Mie calculations for spherical ice particles with a refractive index 1.311 at a photon wavelength of 0.55 μm (Warren 1984), and the contrail thickness l. The value $l = 1.5$ m is a reasonable estimate for the jet diameter at the distance $x \approx 30$ m of interest. Visible but faint cirrus clouds are characterized by $\tau_v \gtrsim 3 \times 10^{-2}$, depending on wavelength, illumination conditions, viewing angle, and distance, hence optical depths larger than this lower limit can serve as a second, independent visibility criterion.

Figure 5 presents important results of this investigation, namely the temporal evolution of the contrail's optical depth for $r_0 = 0.02$ μm, $\alpha = 0.1$, and for ice particle number densities n ranging from 10^3 to 10^7 cm^{-3}. The vertical dashed line indicates the time $t_v = 0.3$ s within which the contrail is first observed. (We neglect the first 0.01 s up to the point when the plume becomes supersaturated.) For small values of n,
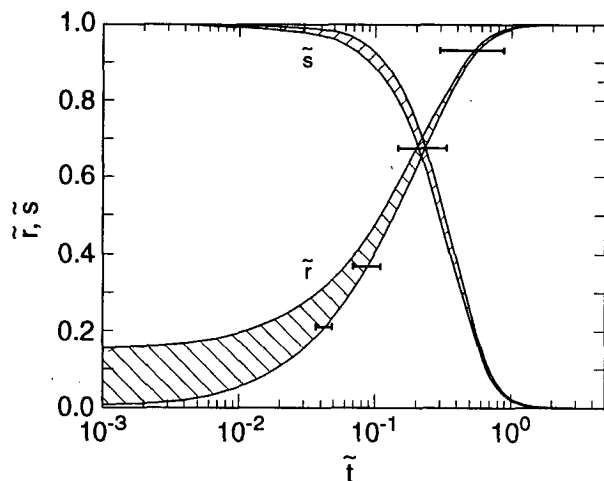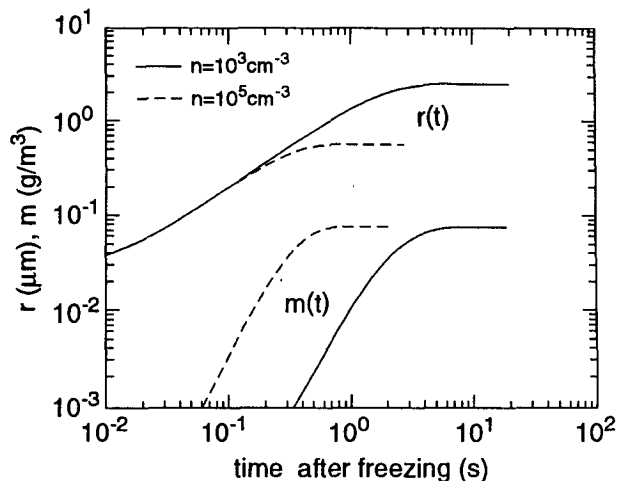

FIG. 3. Scaled solutions of the initial growth phase model for ice particles in nascent contrails. The solid lines show their radius $\tilde{r}$ and the ice supersaturation $\tilde{s}$ vs the time $\tilde{t}$ after freezing, for $\alpha = 0.5$ and $\tilde{r}_0 = 0$. The shaded region displays changes of the solutions when $\tilde{r}_0$ is varied in the range $\tilde{r}_0 = 0 - 0.15$. The horizontal bars indicate changes of the solution when α is varied from 0.1 (left ends) to 1 (right ends).
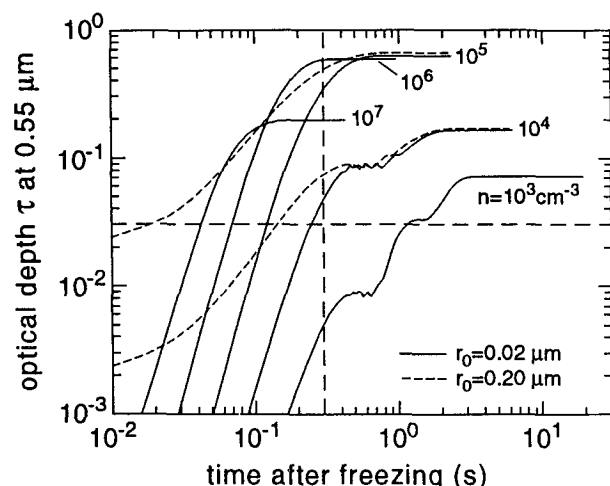
FIG. 5. Optical depths τ at 0.55 μm of the ATTAS contrail vs time t after freezing for various ice particle number densities n for initial radii $r_0 = 0.02$ μm (solid lines) and $r_0 = 0.2$ μm (dotted lines, only for $n = 10^4$ and 10^5 cm^{-3}). We use $\alpha = 0.1$. The vertical and horizontal dashed lines mark the time past exit when the contrail first became visible and the minimum optical depth required for visibility, respectively.

the crystals need a relatively long time to grow to sizes large enough to impact the optical depth, the evolution of which reflects the oscillating behavior of the scattering function Q_{ext} with increasing r. The maximum optical depths increase with increasing values of n, although the maximum radii become smaller. (This behavior is reversed for $n > 10^5$ cm^{-3} and $r_{max} < 0.6$ μm, when the particle radius becomes too small and scattering is less effective.) The horizontal dashed line marks the value τ_v required for visibility. The dotted curves for $n = 10^4$ cm^{-3} and $n = 10^5$ cm^{-3} were obtained with $r_0 = 0.2$ μm, showing that this choice has a significant influence on the evolution of τ for times < 0.3 s after freezing. (Note that for r_0 significantly smaller than 20 nm, the initial growth phase would last longer because such particles would be less supersaturated due to an enhanced Kelvin barrier. Investigation of the Kelvin term shows that freezing nucleation is inhibited for particles with radii smaller than $\approx 2-4$ nm.) From Fig. 5 we conclude that around 10^4 cm^{-3} particles with radii of about ~ 20 nm must have been present initially in order to grow to a visible contrail within the time window given by the ATTAS observations. This lower bound could be somewhat relaxed (by about a factor 2) if we allow for larger soot particles. (When setting $\alpha = 1$ or $\alpha = 0.04$, the lower bound is shifted to 10^3 cm^{-3} or 10^5 cm^{-3}, respectively.) We note that this estimate is consistent with Appleman's visibility criterion based on the ice water content.

The present model is easily applied to contrails from other airplanes: especially, the results support the conclusion drawn by Kärcher et al. (1995), based upon

numerical simulation of nucleation and condensation processes in a B747 plume, that below the water saturation threshold, homogeneous freezing of aqueous sulfuric acid droplets probably does not lead to visible contrail formation (see section 3b).

3. Primary contrail particles

In this section, we characterize the three primary aerosol types in young contrails (cp. Fig. 1) with respect to typical size distributions and abundances, to find out which of them may serve as a potential source for ice particles.

a. Background aerosols

Typical upper-tropospheric aerosols are characterized by total number densities between 1 and 100 cm^{-3} and typical radii between 0.01 and 0.1 μm, with high variability in the abundances for smaller aerosols and less pronounced variations for the larger particles (Talbot et al. 1992; Pueschel et al. 1994). Total condensation nuclei (CN) number densities exceeding 1000 cm^{-3} have to be considered as extreme cases. Also during the ATTAS flights, plume particles were much more abundant than background aerosol.

b. Volatile aqueous sulfuric acid droplets

Using our trajectory box model (Kärcher et al. 1995, 1996) we could show that homogeneous freezing of H_2SO_4/H_2O droplets generated in situ does not lead to visible contrail formation when temperatures approach the Appleman threshold condition, because predicted ice particle concentrations are too low and freezing timescales too long. This also holds for the ATTAS contrail. Moreover, this ice formation process should show a strong dependence on the fuel sulfur content, which was not observed by Busen and Schumann (1995): they detected no visible difference in the contrails either using very low (0.002 gS/kg fuel) or rather high (0.26 gS/kg fuel) sulfur contents in the jet fuel.

However, when the plume becomes supersaturated with respect to water, homogeneous freezing could, in principle, compete with heterogeneous processes. To check the possible importance of homogeneous ice formation we apply our numerical model to the case with lower air temperature $T_a = 222.95$ K and higher relative humidity $RH_a = 45\%$, which leads to a maximum relative humidity of 105%. For this case we compute cumulative number densities of aqueous H_2SO_4 droplets, n_d. In the calculation, water depletion from the gas phase due to ice particle formation is suppressed; hence, the droplet abundances calculated in this way are upper bounds. The results for a fuel sulfur content of 0.26 g S per kg fuel are shown as solid lines in Fig. 6 for n_d ($r_d > 50$ nm) and n_d ($r_d > 100$ nm), with the droplet radius r_d. Also shown are the corresponding

homogeneous freezing times (dashed lines, calculated as $\tau_{hom}^{frz} = 3/(4\pi r_d^3 J_{hom}^{frz})$, where J_{hom}^{frz} is the homogeneous freezing rate). Clearly, the maximum droplet number density of 10^{-3} cm^{-3} is at least seven orders of magnitude smaller than required by the visibility analysis. At the same time the freezing of these droplets is too slow. Smaller droplets, although present in much higher abundances, do not freeze homogeneously within 0.1 s. Hence, these calculations suggest that homogeneous freezing of H_2SO_4/H_2O droplets cannot be an important pathway of visible contrail formation, even if the plume is slightly supersaturated with respect to water. Figure 6 also shows n_d ($r_d > 50$ nm) for a run with 5.5 g S per kg fuel, which is well above the internationally accepted sulfur content in kerosene (upper solid line). Under these extreme conditions number densities of droplets that could freeze homogeneously exceed 1000 cm^{-3}, indicating that homogeneous freezing can then indeed compete with heterogeneous mechanisms, especially at even lower ambient temperatures. Interestingly, in a follow-on measurement with the AT-TAS, Schumann et al. (1996) observed an earlier onset of contrail formation for these very high sulfur levels (the ambient temperature was 5 K below Appleman's threshold and the corresponding freezing timescales were shorter than those shown in Fig. 6).

Another mechanism that could increase the ability of the droplets to freeze homogeneously is the possibility

time after emission (s)

FIG. 6. Cumulative number densities n_d of volatile H_2SO_4/H_2O droplets with radii $r_d > 50$ nm and $r_d > 100$ nm nucleated in the ATTAS jet plume vs x on the jet axis $y = 0$ for high (lower solid lines) and very high (upper solid line) fuel sulfur contents. The dashed lines mark the homogeneous freezing timescales τ_{hom}^{frz} of 50- and 100-nm droplets. Freezing nucleation was not included in these simulations. Similar processes evolve off the jet axis in the mixing region, but shifted to maximum distances below 30 m (or times below 0.5 s after emission, see upper axis) behind the nozzle.

TABLE 1. Gas phase budgets relevant for heterogeneous chemical processing. Exit plane abundances for OH, NO_2, and SO_2; peak number densities for HNO_3 and H_2SO_4; number of monolayers ML; and absorbed mass μ per mass of a soot particle according to (9) with 20-nm radius after 0.1 s (for OH: after 10 ms). Conversion rates of 4% of emitted NO_2 into HNO_3 and of 0.5% of emitted SO_2 into H_2SO_4 are assumed.

Species	n_{max}, cm^{-3}	ML	μ, %
SO_2[a]	4.5×10^{10}	0.09	0.4
H_2SO_4[a]	2.25×10^8	0.0003	0.003
SO_2[b]	1.2×10^{13}	24	95
H_2SO_4[b]	6×10^{10}	0.12	0.7
SO_2[c]	2.5×10^{14}	500	1984
H_2SO_4[c]	1.25×10^{12}	2.5	15.2
OH[d]	3.6×10^{13}	2.4	2.5
NO_2[e]	4×10^{13}	80	228
HNO_3	1.6×10^{12}	3.2	12.5

[a] Emission index 0.002 gS/kg fuel (low).
[b] Emission index 0.26 gS/kg fuel (high).
[c] Emission index 5.5 g S/kg fuel (very high).
[d] Corresponds to an estimated value of 10 ppmv.
[e] Based on a NO$_x$ emission index of 10 g NO$_2$/kg fuel, splitted into 10% as NO_2 and 90% as NO. As for OH, estimates of the fraction [NO$_2$]/[NO$_x$] at the exit plane are uncertain.

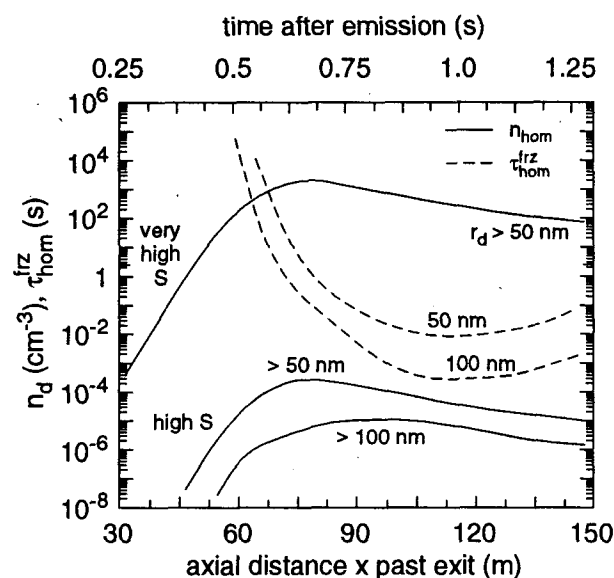that they take up large amounts of HNO_3 during cooling. Table 1 gives the chemical budget of the ATTAS exhaust based on the chemical/microphysical box model presented by Kärcher et al. (1995). It shows that the HNO_3 emission is about 27 times greater than that of H_2SO_4 in the case with 0.26 g S per kg fuel. Using the vapor pressure expressions given by Luo et al. (1995), we estimate the HNO_3 uptake by the droplets assuming thermodynamic equilibrium (i.e., ignoring kinetic effects and the Kelvin term, which both can substantially slow down HNO_3 uptake). We find that at the onset of ice supersaturation (at 233 K) the ternary aerosol would contain 29 wt% HNO_3, 68 wt% H_2O, and only 3 wt% of H_2SO_4. This uptake depletes the HNO_3 in the gas phase to about 45%. For comparison, if no HNO_3 is allowed to enter the binary aerosol under the same conditions the ternary aerosol would consist of 67.5 wt% H_2O and 32.5 wt% H_2SO_4 (all numbers assuming thermodynamic equilibrium conditions). The ratio of volumes of these droplets is related to the H_2SO_4 weight fractions (W) via $V_{ternary}/V_{binary} = W_{binary}/W_{ternary} \approx 11$ — that is, an increase in radius by about a factor 2.2. However, inspection of Fig. 6 shows that the droplets even after this substantial growth are unlikely to satisfy the visibility criterion: an increase by a factor of 2 in the radius increases the abundance by only 1–2 orders of magnitude. Hence, the effect of HNO_3 on the homogeneous contrail formation is much smaller than increasing the sulfur content from 0.26 to 5.5 g S per kg fuel. While additional sulfur directly enhances homogeneous nucleation and early droplet growth, the nitric acid comes into play only at rather late times when its solubility in the H_2SO_4 solution increases.

It should be noted that we used a box model representing on-axis conditions (Kärcher 1995) to calculate Fig. 6. On the other hand, as stated in section 2a, contrails will be initiated off the jet axis. However, we believe that the microphysical processes evolve quite similarly at any radial distance in the jet, with the exception of a somewhat earlier onset of nucleation and growth in the jet mixing region, so that similar abundances as shown in Fig. 6 will be observed at much smaller axial distances in the mixing region (typically three times earlier than on axis, cp. section 2a). This reasoning also applies to the results presented in section 4. Precise modeling of the onset of contrail formation at threshold conditions would require a full two-dimensional treatment which at present is not available.

c. Soot particles

Soot particles are created from the vapor phase during fuel combustion at high temperatures in regions with low oxygen abundances and leave the jet engine as porous spheres or nearly spherical clusters (Wagner 1978). Various measurements of jet engine exhaust aerosols have been performed by Rosen and Greegor (1974), Hagen et al. (1992, 1994), Whitefield et al. (1993), and Schumann et al. (1996). Both combustion aerosols in the laboratory and particulates collected under cruising conditions in the upper troposphere showed similar characteristics. To a good approximation, the soot particles are distributed lognormally, truncated at some minimum and maximum radius, with exit plane number densities of 10^6 cm^{-3} (10^5 cm^{-3}), mean radii $r_s = 20$ nm (100 nm), and half-widths 1.4 (1.8) for lean (rich) jet fuel combustion stoichiometry (Whitefield et al. 1993). Schumann et al. (1996) pointed out that their experiment is compatible with emission indices as large as 0.5 g soot per kg fuel and soot radii of 30 nm. Using the values for lean combustion and a density of 2 g cm^{-3} and assuming a smooth spherical surface without accounting for the porous structure of the nascent particulates, we calculate a specific surface area of 75 m^2 g^{-1}, a total mass of 4×10^7 g mol^{-1}, or 3.4×10^6 carbon atoms per soot particle, and an emission index of 0.028 g soot per kg fuel for the ATTAS aircraft, in good agreement with literature data (e.g., Goldberg 1985, 27) and recent evaluations (Stolarski and Wesoky 1993). Our calculations reveal that the initial soot number density diluted to a few percent at the time of freezing, depending on the exact radial location of contrail onset. If a large fraction of the soot particles could freeze, ice crystal number densities would be above the lower limit given by the visibility criterion.

Aging soot particles slowly coagulate on a timescale greater than 10^4 s and form micron-sized straight or branched chains. Hagen et al. (1991) found scavenging of such combustion aerosols to occur at faster rates than predicted by Brownian coagulation theory and Hallett

and Oraltay (1988) pointed out the change in morphology of growing or evaporating ice crystals in the presence of soot. Both findings could be important for modeling the lifetimes of persistent contrails and their impact on heterogeneous chemistry and radiative balance.

d. Summary

We conclude that under threshold conditions for contrail formation, when the plume becomes supersaturated with respect to ice but not water, a large fraction of the soot particles has to be activated and grow ice leading to an observable contrail, for this is the only primary particle type which is present in sufficiently high abundances by the time of freezing. This result seems to be in contrast to the findings of Blake and Kato (1995), who on the basis of measured soot abundances and hemispheric mass balance calculations suggest that aircraft soot injected at altitude does not represent a significant source of CN for sulfuric acid aerosols. (We note, however, that these authors discuss possible far-field effects of soot, whereas we investigate its role in contrail formation.) Both the ATTAS experiment by Busen and Schumann (1995) and our flow field calculation show that a contrail should become visible below the water saturation threshold, thus extending the classical formation criterion discussed by Appleman (1953) to higher threshold temperatures (for a given ambient relative humidity and pressure). Only when ambient temperatures fall sufficiently below Appleman's threshold criterion, homogeneous freezing of solution droplets may compete with heterogeneous freezing. Our findings are also supported by the experimental evidence that ice crystals in contrails observed nearby natural cirrus (and likely to be formed on exhaust particles), are higher in abundance, initially of uniform size distribution, and smaller than cirrus crystals (Gayet et al. 1996).

4. Activation of soot particles

Soot particles could dramatically facilitate contrail formation if their surface can be activated to a considerable degree. The main obstacle for the droplets to grow is the Kelvin barrier that enhances the vapor pressure of species in the solution by a factor $\exp(2\sigma v_i / RT r_d)$, where σ is the surface energy of the solution, v_i is the molar volume of species i, $R = 8.31$ J (mol K)$^{-1}$ is the universal gas constant, and r_d is the droplet radius. Typically, $r_d \leq 1$ nm for freshly nucleated droplets and the Kelvin term enhances the vapor pressures by more than an order of magnitude. However, if a part of a soot particle is wetted, the radius of curvature increases and ideally approaches the radius of the substrate (20 nm), in which case pressure enhancement due to the Kelvin term is only about 10%.

While the nature of active sites of industrial black carbons used to remove impurities from gases or so-

lutions has been extensively studied, we have no precise information about the processes that lead to a possible activation of the soot particles within the combustor and under atmospheric conditions. There have been a few investigations concerning the suitability of soot as cloud condensation nuclei (CCN) or as ice forming nuclei (IN) (e.g., Hallett et al. 1989; DeMott 1990; Pitchford et al. 1991; Whitefield et al. 1993) and of gas–soot interaction (Thlibi and Petit 1994; Wyslouzil et al. 1994), but these were performed at quite different conditions so that the results cannot be directly applied to our problem. Moreover, the measurements indicate a large range of CCN/CN ratios of soot varying from $1/1000$ (Pitchford et al. 1991) up to $1/3$ (Whitefield et al. 1993).

In the following, we investigate the possibility of wetting the aircraft-induced soot particles and discuss possible activation pathways under plume conditions. We discuss contact angle measurements and freezing experiments carried out to address the questions of activation of graphitic surfaces by OH exposures and freezing of sulfuric acid hydrates induced by rapid plume cooling. Finally, we estimate binary heterogeneous nucleation rates of H_2SO_4/H_2O droplets on the soot particles and heterogeneous freezing rates within the framework of the classical theory.

a. Water uptake on a carbon surface

In the absence of any detailed knowledge about the surface properties of the soot particles, we investigate, as a first step, the adsorption and desorption rates of water molecules on a nonporous, graphitized carbon black surface. An example of such an essentially oxygen-free, hydrophobic particulate is Graphon, for which water adsorption isotherms and heats of adsorption have been measured in the past (Young et al. 1954; Millard et al. 1955). Studying the wetting behavior of such a hydrophobic system gives a lower bound for the fractional coverage Θ_{ads} of water molecules on the surface of jet engine exhaust particulates.

The maximum number of adsorbed water molecules per unit area of the surface is given by $\sigma_0 = 1/d^2 = 8.2 \times 10^{14}$ cm^{-2}, where $d = 0.35$ nm is the diameter of an H_2O molecule. The impingement rate of the vapor to the soot particles with radii r_s in the free molecular regime is given by $\beta_w = j_w/(4\pi r_s^2) = n_w \bar{v}_w/4$, with j_w from (2) with $\alpha = 1$, the thermal velocity $\bar{v}_w = [8k_BT/(\pi m_w)]^{1/2}$ at the local plume temperature T, and the Boltzmann constant $k_B = 1.38 \times 10^{-23}$ J K^{-1}. The rate of adsorption then is $(1 - \Theta_{ads}) \cdot \beta_w/\sigma_0$, where the factor $(1 - \Theta_{ads})$ accounts for surface saturation effects. Following de Boer (1968, 44), the rate of desorption is given by Θ_{ads}/τ_w, where τ_w represents the average time the vapor molecules stick to the surface before evaporating. Clearly, this time depends on the substrate's ability to dissipate the energy of the incoming molecule and depends on temperature via $\tau_w = \tau_0$

$\exp[Q/(RT)]$, where Q is the heat of adsorption. The time τ_0 can be estimated by means of statistical mechanics and is related to the loss of entropy upon adsorption from the vapor state. It may be shown equal to $h/(k_BT) \cdot f(\mathscr{Z})$, where $h = 6.63 \times 10^{-34}$ J s is Planck's constant and $f(\mathscr{Z})$ is a function of the partition functions $\mathscr{Z}$ of translation, rotation, and vibration of the molecules in the gaseous and adsorbed state. Mobile adsorption with rather long adsorption times $\tau_0 = h/(k_BT)$ of the order of 10^{-13} s is obtained whenever an adsorbed molecule lost only one degree of freedom of translation upon adsorption, retaining all other degrees of freedom. In contrast, localized adsorption (like for water on graphite) is characterized by small values of τ_w of the order of 10^{-16} s. The rate equation governing Θ_{ads} finally reads

$$\frac{d\Theta_{ads}}{dt} = -\frac{\Theta_{ads}}{\tau_w} + (1 - \Theta_{ads})\frac{\beta_w}{\sigma_0}. \qquad (8a)$$

Following Hamill et al. (1982) and de Boer (1968, p. 235), we use $Q = 45.2$ kJ mol^{-1} and $\tau_0 = 2.4 \times 10^{-16}$ s for water on carbon, in agreement with the experimental findings for Graphon. Inspection of (8a) shows that water adsorption and desorption processes are in a quasi steady–state on the timescale 10^{-2} s over which plume temperature and water vapor abundance decrease, that is, $d\Theta_{ads}/dt \approx 0$, which leads to the Langmuir-type coverage

$$\Theta_{ads} = \frac{\beta_w \tau_w/\sigma_0}{1 + \beta_w \tau_w/\sigma_0}, \quad \frac{\beta_w \tau_w}{\sigma_0} = \frac{n_w \bar{v}_w \tau_0}{4\sigma_0} \exp\left(\frac{Q}{RT}\right). \qquad (8b)$$

This expression is evaluated at the local plume temperature $T(x, y)$ and water vapor density $n_w(x, y)$. Fig-
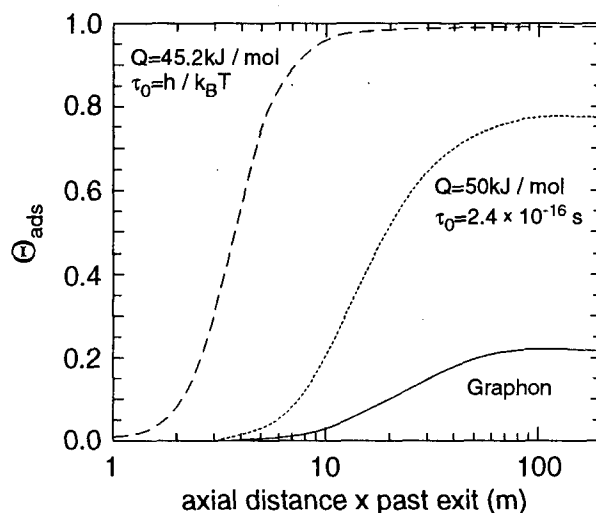
FIG. 7. Fractional coverage Θ_{ads} of water on a pure carbon surface (Graphon, solid line) and on successively more hydrophilic (activated) particles (dotted and dashed lines) vs x along the jet axis.

ure 7 displays the fractional coverage Θ_{ads} for the particles in an air parcel leaving the ATTAS jet engine on a trajectory along the jet axis ($y = 0$) as a function of x. The case just discussed is shown as a solid line, leading to a 10% coverage of the soot particles with water molecules about 20 m behind the exit, and a maximum 22% coverage at about 100 m. To investigate the sensitivity of the water adsorption on the underlying parameters, we evaluate (8b) using $\tau_0 = h/(k_B T)$ ≥ 2.4×10^{-16} s (dashed line) and $Q = 50$ kJ mol^{-1} (dotted line), respectively, which may represent the surface properties of soot particles activated by the high OH radical concentrations and being more water receptive than pure carbon (cp. section 4c.1 below). These results suggest that sufficiently hydrophilic soot particles can acquire a substantial fraction of a water monolayer within 10 m behind the engine, even along the jet axis where the relative humidity increases later than in the mixing region.

The partial water coverage of these soot particles should render them more hydrophilic. This enhances the sticking of other molecules like H_2SO_4 and HNO_3, in particular since the available water should facilitate their dissociation. This would shift the emphasis from a physical adsorption concept to a chemisorptive mechanism, and the resulting higher heats of adsorption (Q values typically above 100 kJ mol^{-1}) could easily balance the effect of lower molecular concentrations, see (8b). The chemisorption, in turn, may facilitate heterogeneous nucleation and more rapid growth of solution droplets and at a later stage heterogeneous freezing of ice crystals.

b. Chemical processing of soot particles

To fulfill the visibility criterion (section 2d) a large fraction of the soot particles must possess a sufficient number of active sites, which allow them to grow droplets large enough to overcome the Kelvin barrier. From the highly simplified picture discussed with the help of Fig. 7, however, it remains open to which degree the carbon particulates must be processed by exhaust trace species other than H_2O in order to become water receptive and to promote freezing nucleation. It is therefore helpful to investigate for which species the transport from the gas phase to the surface of the soot particles might be kinetically limited. Among the primary and secondary exhaust products, strongly absorptive species in the gas phase are O_2, NO_x, SO_2, OH, HNO_3, and H_2SO_4, the latter being the most water soluble species. Nitric and sulfuric acid are mainly built up by OH-induced oxidation of their precursors NO_2 and SO_2 within 20 ms in the gas phase of the very young aircraft plume (Miake-Lye et al. 1994; Kärcher et al. 1996). Since nitrogen and sulfur dioxide are chemically not significantly depleted, they are diluted almost like inert tracers. In contrast, the lifetime of the hydroxyl radical is limited to a few milliseconds. Typically, the number

densities of these species exceed the background levels by many orders of magnitude during the first seconds of plume dispersion. In Table 1, we list their peak concentrations n_{max} for the ATTAS jet engine. Also given is the number of monolayers, ML, after $\Delta t = 0.1$ s ≤ t_v (for OH: after 10 ms) on the soot particles (assuming a sticking probability of unity) and the resulting masses μ relative to the soot mass (both are upper bounds because in these estimates we neglect the dilution of the plume and the time necessary for the chemical production of the acids). The table is calculated from

$$\text{ML} = \frac{\beta \Delta t}{\sigma_0}, \quad \mu = \text{ML} \cdot \frac{3}{\rho_s r_s} \sigma_0 m, \qquad (9)$$

where $\beta = n_{max}\bar{v}/4$ is the impingement rate and m the molecular mass for each trace gas. The peak number densities n_{max} for NO_2, SO_2, and OH are essentially given by their emission indices (or exit plane abundances), and for the acids we estimate that at most 4% of the initial NO_2 and 0.5% of the initial SO_2 is converted into nitric and sulfuric acid, respectively (Kärcher et al. 1996). For the soot particles, we use a mean radius of $r_s = 20$ nm and a mass density of $\rho_s = 2$ g cm^{-3}. We assume $\sigma_0 = 5 \times 10^{14}$ cm^{-2} for the maximum number of molecules that can be adsorbed per unit area of the substrate and a fixed mean thermal speed of $\bar{v} = 4 \times 10^4$ cm s^{-1} for each species, for simplicity. In Table 1 we list results for three different fuel sulfur contents (low, high, and very high), corresponding to those realized in the ATTAS experiments. Obviously, the nitrogen species and the hydroxyl radical have a great potential to interact with the soot particles immediately behind the jet engine. The same holds for sulfur dioxide, which is present in such high abundances that it could in principle produce at least 9% of a monolayer. However, gaseous sulfuric acid can cover only the soot particles when the sulfur content of the kerosene is very high. No visible difference in the formation and appearance of contrails has been found in the cases with 0.002 and 0.26 g S per kg fuel, while the case with very high sulfur content showed an earlier onset of contrail formation. Hence, it is unlikely that the soot particles in the former cases became directly activated by gaseous H_2SO_4. There are two alternative mechanisms: either HNO_3 is the main agent leading to sufficient growth of the droplets on the soot particles, or SO_2 becomes heterogeneously converted into H_2SO_4 by surface reactions. Once sulfuric or nitric acid is present on the surface and the relative humidity is sufficiently high, aqueous solution droplets or even a full coating will cover the soot particles, which eventually freeze heterogeneously as water ice.

The catalytic activity of black carbon surfaces is a well-known phenomenon (Goldberg 1985, 86). Black carbon appears effective in catalyzing SO_2 oxidation with light, ozone, oxygen, and nitrogen oxides. In analyzing airborne aerosol samples from the Kuwait oil

fire plumes, Parungo et al. (1992) found that the dominant particles were agglomerates of spherical soot particles coated with sulfate, probably through catalytic oxidation combined with heterogeneous nucleation. Numerical investigations by Middleton et al. (1982) indicate that black carbon catalyzed reactions make up a significant contribution to the sulfate production in the atmosphere. In the context of contrail formation, it could be of particular importance that heterogeneous reactions on the surface of the soot particles may occur through synergistic effects among various trace gases. The observations of Schryer et al. (1980) demonstrate that when both SO_2 and NO_2 in dry air are exposed together to a carbon black, strong chemisorption converts the SO_2 into sulfate, with NO_2 as the oxidizing agent. Cofer et al. (1980) pointed out that such reactions are also operative at a relative humidity of 65%. As reported by Goldberg (1985, 96), sulfate yields due to heterogeneous interactions of SO_2 and NO_x with black carbons may become considerably enhanced with increasing temperature and heating of the carbon substrate. Clearly, more experimental work is needed to clarify what degree of heterogeneous processing and how much deposition of trace species is needed to activate the soot particles and which catalytic processes are at work under aircraft plume conditions. It will then be essential to use fresh soot resulting from jet fuel combustion, because the carbon particulates could already become processed at the much higher temperatures and radical concentrations within the combustor, where they might already acquire a certain sulfur mass fraction.

c. SO_2 versus HNO_3 uptake

In the last section we have argued that besides the uptake of water onto the soot surfaces it might be additional uptake of HNO_3 and SO_2 with subsequent oxidation to H_2SO_4 leading to soot activation, while uptake of H_2SO_4 from the gas phase alone is not efficient due to its low abundance. For another trace gas present in sufficient amounts, nitrogen dioxide, there is no obvious oxidation path leading to HNO_3; hence, it is less likely to contribute directly to the coverage, rather does it act as an oxidizer of SO_2 to form H_2SO_4.

These conclusions were reached based on a simple mass budget analysis of the trace gases available in the exhaust. We will now further investigate the pathways of HNO_3 uptake and SO_2 oxidation in the light of two observations; first, the ATTAS observations described above and second, direct particle measurements by Hagen et al. (1992) behind jet engines.

During the ATTAS experiments no difference was observed in contrail formation when burning low or high sulfur kerosene (cases a and b in Table 1), only when sulfur contents were far above internationally accepted values (case c in Table 1) the contrail showed an earlier onset. As discussed above, this is in agreement with the abundance of H_2SO_4, which only in case c is high enough to cover the particles with more than one monolayer. Moreover, this observation could be explained in terms of HNO_3, which has the potential to form more than one monolayer, and only in case c there is enough H_2SO_4 to compete with HNO_3 and to facilitate contrail formation. However, the observation is not in agreement with a fast and substantial oxidation of SO_2 to H_2SO_4, because if this took place we would not expect a difference between cases b and c in view of the high SO_2 concentrations in both cases.

On the other hand, there are the measurements by Hagen et al. (1992), who collected particles directly behind a jet engine. Their analysis of the hydration properties of fresh combustion aerosols revealed that they do contain soluble material and are fairly monodisperse in terms of soluble mass fraction, which amounts to 8%–10%. The main difference in the interpretation of these measurements as compared to the ATTAS observations is that the aerosol sampling took place only 2.5 m behind the exit plane, which corresponds to only ~0.01 s after emission. Hence, the monolayer (ML) and mass fraction (μ) values have time to develop only to about 10% of the values given in Table 1. These measurements, if no coverage took place at later times within the measuring device, clearly speak against the HNO_3 coverage hypothesis, not only because there is not enough HNO_3 to rapidly enough build up the observed volatile mass fractions of 8%–10%, but also because 0.01 s after emission the exhaust is still too hot ($T \approx 400$ K) for HNO_3 condensation. Clearly, this requires the participation of SO_2 or an unidentified additional pathway for explanation. However, at such high temperatures even the condensation of H_2SO_4 is not yet effective, so that we find no obvious explanation for the soluble mass fractions observed by Hagen et al. (1992).

Using the concept of rapid adsorption of various exhaust gases the experiments by Busen and Schumann (1995) and Schumann et al. (1996) and by Hagen et al. (1992) cannot be explained without contradiction. At present both mechanisms, direct adsorption of HNO_3 and adsorption of SO_2 with subsequent oxidation to H_2SO_4, must be considered as possible pathways of contrail formation.

d. Experimental

In contrail modeling there are two microphysical issues of technical nature that allow a straightforward experimental clarification. First, for the calculation of heterogeneous nucleation rates of H_2SO_4/H_2O droplets on soot using classical nucleation theory, we need an estimate of the contact angle of the solution droplets on the soot surface (cp. section 4e). A measurement of the contact angle should take account of the possibility of efficient surface activation due to the high concentrations of OH radicals in the exhaust. As we will

show below, even activated carbonaceous surfaces do not show a good compatibility with the acidic solution. Second, the rapid cooling of the exhaust might cause the solution droplets to freeze out hydrates due to heterogeneous nucleation on the soot surface before the droplets are supersaturated with respect to ice. In particular, sulfuric acid tetrahydrate ($H_2SO_4 \cdot 4H_2O$, SAT) is a potential candidate for hydrate formation (Luo et al. 1994). Such a freezing could, in principle, completely change the further evolution of contrail formation, but, as we show below, the freezing rate is extremely low, hence the freezing probability almost negligible.

1) MEASUREMENTS OF CONTACT ANGLES

To determine contact angles of solution droplets on selected surfaces we use a modified microscope (35-mm lens). Several methods to obtain suitable soot surfaces have been investigated. For example, the soot was directly collected from flames. Alternatively, a suspension of powderized graphite in an ammonia solution was brought onto the microscopic slide, producing a thin soot layer upon drying. However, in both cases the soot coating was very porous, enabling the solution to diffuse into the layer. This could be avoided by chosing a commercially available graphite laminate (Sigraflex by Sigri) made from natural graphite. The regular surface of the laminate supports solution droplets without apparent diffusive or chemical interactions.

The solution droplets were prepared from concentrated sulfuric acid (96.5 wt%). After equilibration with the ambient conditions the droplet size was determined using an external scale on the microscopic slide. The equilibrium concentration of the H_2SO_4 solution was estimated to be 45 ± 5 wt% and the dependence of the contact angle on the concentration of the solution is assumed to be very small. The meniscus of the droplet on the graphite surface was brought into focus and a picture was taken with about 100-fold magnification. The contact angle θ was calculated according to the formula $\cos(\theta) = (L^2 - 4H^2)/(L^2 + 4H^2)$, where L and H are the length and the height of the droplet, respectively, as taken from the photograph (see Fig. 8a). The contact angle for the H_2SO_4/H_2O droplet with about 50 wt% on the graphite surface is determined to be 64° ± 2°.

As mentioned above, the soot particles in the jet plume are exposed to high concentrations of OH radicals and other oxidizing trace gases. To mimic these conditions, we activated the graphite laminate in an OH-containing atmosphere. This was realized by expanding the vapor phase over a diluted H_2O_2 solution into a reaction flask, which then was illuminated by a mercury vapor lamp. The radiation leads to a production of about 10^{11} cm^{-3} s^{-1} OH radicals, which under equilibrium conditions are balanced by the OH self-reaction (leading back to H_2O_2) and by heterogeneous
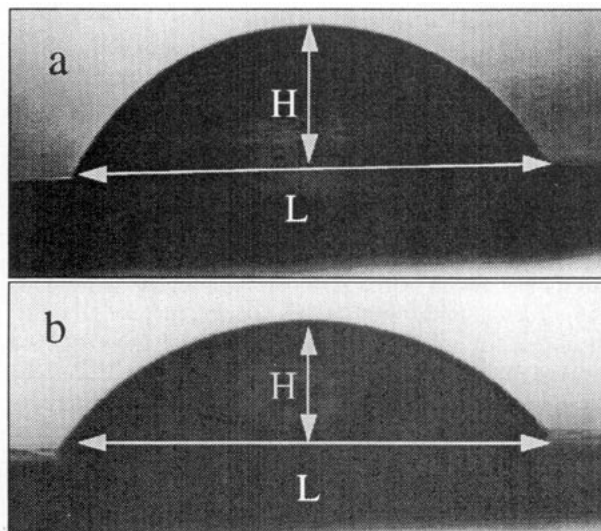

FIG. 8. Microscope photography of a 1-mm H_2SO_4/H_2O solution droplet on (a) graphite laminate and (b) oxidized graphite laminate. The contact angle decreases by 10° as the surface becomes more hydrophilic due to ·OH radical oxidation.

losses of OH on the graphite laminate and the flask walls. If equilibrium was established only by the OH self-reaction, we estimate an OH concentration of about 5 ppbv. As we held the graphite laminate for 1 h in this atmosphere, the product of OH number density and exposure time ($n_{OH}\Delta t$) is similar to or higher than that in aircraft plumes, so that comparable activation effects should occur. As expected, the OH-treated graphite surface was more hydrophilic and the contact angle reduced to 55° ± 2°; see Fig. 8b.

2) FREEZING EXPERIMENTS

We performed bulk phase freezing experiments with macroscopic surfaces of graphite and activated carbon to test the freezing properties of soot for the formation of SAT out of a 57 wt% H_2SO_4/H_2O solution (1:4 stoichiometry) at low temperatures.

The setup for these experiments consists of a glass tube with a temperature sensor attached at the outside of the tube for monitoring a possible freezing event. Such events are accompanied by a spontaneous release of latent heat and a corresponding temperature increase of several degrees. The glass tube was held in a liquid ethanol cooling bath to reach the desired temperature, for details see Koop et al. (1995). The solution was prepared from standard chemicals (96.5 wt% H_2SO_4) without further filtering. As representative surfaces, we chose the graphite laminate described above and, alternatively, activated carbon (Aldrich, NORIT A) with a BET surface area of ~ 1500 m^2 g^{-1}. The applicability of the results of these experiments to the contrail situation is limited due to the unknown morphology of the

laboratory samples (cavities, spheroles, and other surface features) compared to that of the fresh soot particles in aircraft plumes. Improvements in this respect will have to wait until in situ measurements of these properties become available.

The freezing experiments show that the 1:4 H_2SO_4 solution with the immersed carbonaceous substrates can be supercooled to very low temperatures without heterogeneous nucleation of hydrates. Temperatures as low as 191 K can be reached and held for many minutes without freezing. From these experiments, we estimate an upper bound of the heterogeneous freezing rate on the carbonaceous surfaces. A freezing event can be caused by several mechanisms: homogeneous freezing of the solution, heterogeneous freezing on the wall of the glass tube, or heterogeneous freezing on the soot-like surface. Because nucleation is a stochastic process, Poisson statistics yields an upper bound of the total freezing rate ω (in s^{-1}) from a single cooling experiment, with $\omega = t_{exp}^{-1} \ln[1/(1 - X)]$, where t_{exp} is the time period over which no freezing was observed and X is the confidence level (e.g., $X = 0.99$ or 99%). An upper bound for the heterogeneous freezing rate J_{het}^{frz} of the liquid in contact with the soot surface area A_s (per unit surface area per second) is then given by $J_{het}^{frz} \leqslant \omega / A_s$. With an estimated value $A_s \doteq 2$ mm^2 of the graphite laminate and $t_{exp} = 15$ min, we determine the upper limit $J_{het}^{frz} \leqslant 7.5 \times 10^{-5}$ mm^{-2} s^{-1}. Similarly, the upper bound for activated carbon (surface area of 1 mg is about 1 m^2) is computed as $J_{het}^{frz} \leqslant 2 \times 10^{-10}$ mm^{-2} s^{-1}. Scaling these nucleation rates to the available surface area of soot in H_2SO_4/H_2O droplets clearly shows that both rates obviously are by far too slow to provide a pathway for the formation of frozen particles down to stratospheric temperatures of 191 K.

e. Binary heterogeneous nucleation

Classical homogeneous nucleation theory predicts very high embryo production rates J_{hom} exceeding 10^{10} cm^{-3} s^{-1} for the binary H_2SO_4/H_2O system in jet aircraft plumes due to large supersaturations, resulting in subnanometer-sized critical clusters as small as 0.7 nm in diameter. The applicability of the theory under plume conditions seems doubtful, as discussed by Kärcher et al. (1995), because hydrated sulfuric acid $(H_2SO_4)_n \cdot (H_2O)_m$ cluster molecules with $n = 1-2$ and $m = 3-5$ can already be regarded as critical germs for the gas-to-liquid phase transition. However, alternative approaches like molecular cluster models or density functional methods, which have been successfully applied to homomolecular nucleation processes in the past, are still out of reach for the binary systems discussed here. Additional uncertainties concerning the morphology of soot and the interaction of the molecular clusters with the surface of the black carbons (as discussed above) come into play. For this reason, we confine ourselves to a comparison of the maximum binary

heterogeneous and homogeneous nucleation rates applied to the ATTAS jet plume. Let J_{het} denote the number of embryos nucleated per unit area of the substrate per unit time and J_{hom} is the number of nucleation events in the gas phase per unit volume of air per unit time. The ratio $\xi = 4\pi r_s^2 n_s J_{het}/J_{hom}$ is given by (e.g., Hamill et al. 1982)

$$\xi \approx 4\pi r_s^2 N_w^{ads} \frac{n_s}{n_w} \exp\left[\frac{\Delta G}{k_B T}(1 - f(\mathcal{M}))\right], \quad (10)$$

where N_w^{ads} is the number of water molecules adsorbed by the soot particles [given by $\Theta_{ads}\sigma_0$ using (8b)], ΔG is the free energy required for the formation of a critical embryo of radius $r_g \ll r_s$, and $\mathcal{M}$ denotes the cosine of the contact angle θ between the germ and the soot substrate. The function $f(\mathcal{M}) = (2 + \mathcal{M})(1 - \mathcal{M})^2/4$ determines the reduction of the free energy required to nucleate germs heterogeneously as compared to the homogeneous case. This classical approach assumes a regular surface structure of the substrate that can be characterized by a single contact angle (Pruppacher and Klett 1978, 268). The effectiveness of the insoluble soot particles for droplet nucleation depends, in our case, merely on the value of $\mathcal{M}$.

We evaluate (10) at conditions where the nucleation rates take their maximum, and for the three different kerosene sulfur emission indices of the ATTAS experiments (cf. Table 1). We take the values for $\Delta G/(k_B T)$ from our homogeneous nucleation calculations, as well as the corresponding peak nucleation rates and droplet abundances. Further, we insert $n_w = 9.7 \times 10^{16}$ cm^{-3} (see section 2a), $n_s = 10^6$ cm^{-3}, $r_s = 20$ nm, and the upper limit for $N_w^{ads} = \sigma_0 = 8.2 \times 10^{14}$ cm^{-2}. The results are given in Table 2 for various values of θ and $\mathcal{M}$, ranging from contact angles 180° ($\mathcal{M} = -1$) to 0° ($\mathcal{M} = 1$), including the angles 64° ($\mathcal{M} = 0.44$) and 55° ($\mathcal{M} = 0.57$) determined experimentally for graphite before and after activation, respectively (see section 4d.1). Table 2 suggests that heterogeneous nucleation rates are several orders of magnitude smaller than ho-

TABLE 2. Heterogeneous vs homogeneous nucleation rates. Ratio ξ of maximum heterogeneous vs homogeneous H_2SO_4/H_2O nucleation rates according to the classical theory (10) at various values for the contact angle θ and $\mathcal{M} = \cos(\theta)$ for the ATTAS jet plume with different kerosene sulfur emission indices. Read 4(−7) as 4×10^{-7}.

θ	180°	90°	64°	55°	0°
$\mathcal{M} = \cos(\theta)$	−1	0	0.44	0.57	1
$1 - f(\mathcal{M})$	0	0.5	0.81	0.88	1
ξ^a	4(−7)	2(−4)	1(−2)	3(−2)	1(−1)
ξ^b	4(−7)	8(−5)	2(−3)	5(−3)	2(−2)
ξ^c	4(−7)	6(−5)	1(−3)	2(−3)	8(−3)

[a] $EI = 0.002$ g S/kg fuel. $\Delta G/(k_B T) = 12.6$.
[b] $EI = 0.26$ g S/kg fuel. $\Delta G/(k_B T) = 10.6$.
[c] $EI = 5.5$ g S/kg fuel. $\Delta G/(k_B T) = 9.9$.

mogeneous gas-to-particle conversion. Both rates become comparable only for a substrate with a much higher compatibility than our experiment suggests.

The result that heterogeneous nucleation does not play a much stronger role is at first sight surprising. From atmospheric considerations one would expect heterogeneous nucleation to dominate homogeneous nucleation under all conceivable circumstances. However, in the young plume conditions are very extreme: supersaturations reach much higher values than in the unperturbed atmosphere and this in turn leads to a very small free energy ΔG of embryo formation. Hence, during nucleation the system does not gain very much energy even if a perfectly suitable surface is available.

We now compute the surface area per soot particle occupied by the total number of nucleated droplets. Upon nucleation, each H_2SO_4/H_2O germ occupies a surface area of roughly πr_g^2, with $r_g = 0.35$ nm. The rate of increase of the area ΔA occupied by germs is given by $\pi r_g^2 J_{het}$; hence, the occupied area per soot particle relative to $A_s = 4\pi r_s^2$ reads

$$\Theta_{nuc} \equiv \left(\frac{\Delta A}{A_s}\right)_{nuc} = \frac{1}{4}\left(\frac{r_g}{r_s}\right)^2 J_{het}\Delta t, \qquad (11)$$

with the time interval $\Delta t \approx 0.2$ s until the gas phase reservoir of sulfuric acid will be depleted by concomitant homogeneous nucleation, which shuts off further gas-to-particle conversion. Table 3 presents the results of (11) for a contact angle of 55°, together with the peak values for J_{hom} needed to compute J_{het} by means of (10). Clearly, for kerosene sulfur levels below average, classical nucleation theory predicts only a small fraction of the surface to be covered with embryonic droplets. In principle, once nucleated, each individual droplet on the surface will grow due to condensation of sulfuric acid and water in the cooling aircraft plume and will reduce the soot surface area available for further nucleation processes. If the growth is fast enough, smaller isolated droplets could merge and eventually the total surface may be covered by a film of liquid sulfuric acid solution. However, guided by our previous study on the condensational growth of volatile solution droplets in the jet plume (Kärcher et al. 1995), we believe that within fractions of a second, this growth mechanism cannot significantly increase the surface coverage (in a plume always subsaturated with respect to water). Especially in the case of low sulfur emission index the majority of droplets stays at subnanometer radii due to the Kelvin barrier and remain highly acidic with typical sulfuric acid weight fractions $W > 0.4$. In contrast, for very high sulfur levels the total area of the soot particles will be covered rapidly by a liquid coating.

The classical rates could be drastically enhanced due to preferred nucleation on chemically activated surface sites (see, e.g., Pruppacher and Klett 1978, 271) and at morphological surface inhomogeneities such as sur-

TABLE 3. Fractional coverage of soot particles. Maximum binary homogeneous nucleation rates J_{hom}^{max} (in cm^{-3} s^{-1}), corresponding number of droplets n_{hom}^{max} (in cm^{-3}), and fractional coverages with droplets either nucleated heterogeneously (Θ_{nuc}) using $\mathcal{M} = 0.6$ or collected by Brownian coagulation (Θ_{col}) per unit surface area of the soot particles for the ATTAS with different sulfur emission indices (in g S per kg fuel).

EI (S)	J_{hom}^{max}	n_{hom}^{max}	Θ_{nuc}, %	Θ_{col}, %
0.002	3×10^8	4×10^7	0.014	0.012
0.26	6×10^{11}	2×10^{10}	5.5	6.1
5.5	4×10^{13}	4×10^{11}	$\rightarrow 100$	$\rightarrow 100$

face discontinuities or capillaries (characterized by very small contact angles or negative curvatures in the classical model) (Fletcher 1969; Gorbunov and Kakutkina 1982). Moreover, the embryos as well as the already nucleated droplets could grow faster by surface migration of adsorbed molecules or by H_2SO_4 production from heterogeneous processing of SO_2. Another activation path could be collection of homogeneously nucleated droplets by thermal coagulation. Every soot particle scavenges droplets (essentially critical clusters present at peak number densities of n_{hom}^{max}; see Table 3) at a rate of Kn_{hom}^{max} per particle, with the coagulation coefficient $K \approx 10^{-7}$ cm^3 s^{-1} for soot particles with radii $r_s = 20$ nm (Fuchs 1964, 288). The peak abundance can be maintained during $\Delta t \approx 0.4$ s and is then reduced by plume dispersion. With the droplet area of πr_g^2 on the substrate, the total surface area occupied by collected droplets ΔA relative to the soot surface area is given by

$$\Theta_{col} \equiv \left(\frac{\Delta A}{A_s}\right)_{col} = \frac{1}{4}\left(\frac{r_g}{r_s}\right)^2 Kn_{hom}^{max}\Delta t, \qquad (12)$$

the larger droplets giving no significant contribution because they are much less abundant. The results of (12) are also given in Table 3, showing similar coverages as a function of the sulfur levels as for the case of heterogeneous nucleation. Also this process has a great potential of activating the soot particles by creating a liquid coating, even when they are considered to be hydrophobic, for fuel sulfur contents well above average.

A detailed modeling study of the various soot activation processes must take into account that multiple heterogeneous nucleation events, subsequent heteromolecular growth of the droplets, and the collection of homogeneously nucleated droplets by coagulation terminate further heterogeneous nucleation as soon as the individual droplets merge and cover the available surface area of the substrate. The availability of gaseous H_2SO_4 for heterogeneous nucleation will be limited by rapid depletion of the sulfuric acid vapor due to homogeneous gas-to-particle conversion.

f. Heterogeneous freezing nucleation

The last section of this paper deals with the heterogeneous freezing process leading to the ice particles, whose growth we treated in section 2. In contrast to heterogeneous gas-to-particle conversion (see section 4e), we will show that freezing nucleation gains considerably from the presence of a surface. Being aware of the well-known uncertainties of the classical nucleation theory for freezing, we use our findings as a qualitative indication that heterogeneous freezing of diluted, nonideal solution droplets containing soot inclusions dominates over direct formation of ice germs from the vapor on the soot surface, rather than as a quantitative estimate. We will apply a modified classical approach to compute the number of nucleated ice germs per unit area of the substrate per second (J_{het}^{frz}), which is slightly adjusted such that it matches other recent calculations (e.g., Jensen et al. 1991; Pruppacher 1995) as well as experimental data and molecular theory results concerning the homogeneous freezing rates all cited by Pruppacher (1995). The overall dependences of the rates on temperature, contact angle, and supercooling, however, remain "classical."

We will assume that soot particles of radii 20 nm are covered either with a liquid film of supercooled water droplets or with an aqueous H_2SO_4 solution and investigate the sensitivity of the freezing timescales $\tau_{het}^{frz} = 1/(4\pi r_s^2 J_{het}^{frz})$ on the contact angle θ between the ice germ and the soot particle. The sulfuric acid weight fraction W of the solution coating is variable and depends on the relative humidity of the cooling jet plume, as discussed by Kärcher et al. (1995), and determines together with the plume temperature T the water activity $a_w(W, T)$ in the acidic solution. Vapor pressures are computed using the model of Luo et al. (1995). Similar to the calculation leading to Fig. 6, in the simulation we do not allow the droplets to deplete the gas phase after freezing.

Figure 9 shows various heterogeneous freezing timescales as a function of the distance past exit for on-axis conditions. The dotted line represents freezing of a droplet with a perfectly wettable nucleus (i.e., for $\theta = 0°$) and gives the highest freezing rates. In this limiting case τ_{het}^{frz} does not depend on a_w, and the activation energy for diffusion of molecules across the liquid-ice phase boundary constitutes the only barrier to nucleation. The dashed and solid lines give the timescales for contact angles of 50° and 90°, respectively, for a pure water coating (lower lines) and for an aqueous H_2SO_4 coating (upper lines). The nucleation rates of the solution droplets are lower (similar to the freezing point depression determined by the water activity). As expected, freezing is more rapid for smaller contact angles. All freezing times decrease with increasing x because the plume temperature decreases and the droplets become strongly supercooled. In addition, the solution
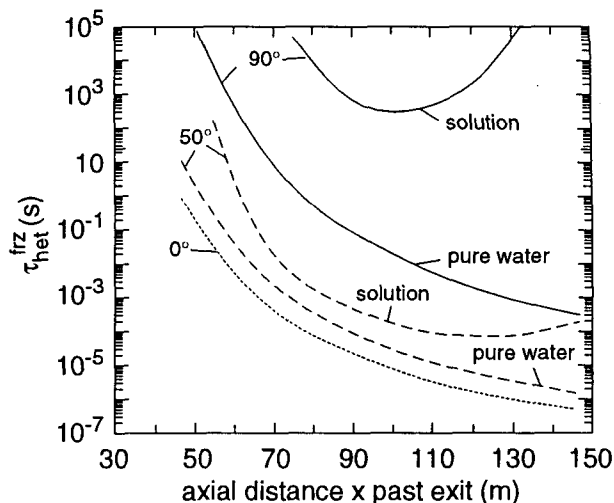

FIG. 9. Heterogeneous freezing timescales τ_{het}^{frz} for soot particles with 20-nm radius vs x at $y = 0$. The lowermost dotted line represents freezing induced by a perfectly wettable, insoluble nucleus. The dashed and solid lines depict τ_{het}^{frz} for contact angles of 50° and 90°, respectively, for a supercooled water (lower lines) and an H_2SO_4/H_2O coating (upper lines) covering the soot particle. The sulfuric acid weight fraction is variable and adjusts to the changing humidity in the cooling plume of the ATTAS.

droplets become more and more diluted due to water uptake, thus increasing a_w. Their values τ_{het}^{frz} increase at later stages, when the temperature and humidity approaches ambient undersaturated conditions and these droplets become again more acidic. Keeping in mind that the freezing rates evolve similarly in the jet mixing region, but merely shifted to approximately three times shorter axial distances, Fig. 9 clearly reveals that for $r_s = 20$ nm, the heterogeneous freezing timescales are sufficiently short for contact angles $< 50°$, even for the solution droplets, being two orders of magnitude shorter than the homogeneous freezing timescales for 50-nm droplets as shown in Fig. 6. Hence, the bulk of all the soot aerosols present can induce freezing, as required by the visibility analysis. Comparing τ_{hom}^{frz} and τ_{het}^{frz} from both figures, we also find that heterogeneous freezing will set in somewhat earlier, possibly reducing the available water vapor rapidly enough to prevent most of the volatile solution droplets from freezing.

We should finally like to note that previous studies have shown the direct nucleation of ice germs from gaseous H_2O on soot particles to be negligible unless ambient temperatures decrease below 210 K (Kärcher 1994). This is easily explained by considering the equation that determines the ice germ radius $r_g = 2\sigma_{ice/vap} v [RT \ln(1 + s)]^{-1}$. Inserting the values given in section 2b, $\sigma_{ice/vap} = 100$ erg cm^{-2}, $v \approx 18$ cm^3 mol^{-1}, $T = T_a = 223.45$ K, and $s = s_0 = 2$, it follows $r_g \approx 2$ nm, or ~ 1000 water molecules per germ. In contrast, the radius of ice embryos in a strongly diluted aqueous solution droplet with $\sigma_{ice/solution} \approx \sigma_{ice/vap}/4$ is only

about 0.5 nm, with correspondingly lower free energies for germ formation and much higher nucleation rates. In agreement with the results discussed above, heterogeneous freezing of solution droplets is clearly favored over the direct gas-to-solid phase transition.

g. Summary

Under conditions above ice but below water saturation, we conclude that at least 20% of the surface area of pure, homogeneous carbon aerosols can be wetted due to adsorption of H_2O molecules under jet exhaust plume conditions. Alternatively, also classical nucleation models predict that the soot particles may acquire a liquid coating, but only for very high fuel sulfur contents. For normal sulfur levels, keeping in mind the time constraint from the visibility analysis, the predicted activation is too small. Besides the possibility that soot might acquire a certain sulfur mass fraction already in the combustor, estimates of various activation pathways operative in the jet regime reveal a great potential for heterogeneous chemical processing of the soot surface, possibly with synergistic effects among the exhaust trace gases. However, it remains unclear whether the emitted HNO_3 or heterogeneously oxidized SO_2 is responsible for the initialization of the observed rapid contrail formation. It is further unclear, due to a lack of knowledge of the surface morphology, to what extent surface effects might enhance the nucleation rates. Assuming the soot particles to be coated by a supercooled liquid, heterogeneous freezing theory predicts sufficiently short timescales for the nucleation of ice germs for contact angles below 50°–60°. The time at which a full or partial coating is established decides upon the liquid growth (which we did not consider here) and final size of the droplets containing soot inclusions prior to freezing.

The fact that we have no detailed knowledge of the surface morphology of fresh soot particulates under plume conditions and that there is no precise information on which heterogeneous chemical reaction pathways (constrained by the short timescales of the jet plume chemistry) lead to active site production at the surfaces of the combustion aerosols will render future applications of nucleation models to describe the activation processes more difficult. It is essential to obtain more experimental data on heterogeneous freezing rates of solution droplets with soot inclusions.

5. Conclusions and outlook

The basic conclusions have already been summarized at the end of each section. The main results of this study are

• Visible contrails behind jet aircraft most likely form below ambient water but above ice saturation, just like natural cirrus clouds. Regions in the atmosphere with conditions supporting contrail formation are larger than predicted with the criterion given by Appleman (1953).

• Around 10^4 cm^{-3} particles with radii greater than ~20 nm must take up the available water vapor and freeze to produce a visible contrail sufficiently close to the airplane. After ice saturation is reached, ice crystals have typical radii around 1 μm. Their further evolution will depend on plume dispersion and background conditions, especially on relative humidity.

• Homogeneous binary nucleation for gas-to-particle conversion and homogeneous ice freezing is not an efficient process and cannot satisfy the visibility criterion under threshold contrail formation conditions.

• The most likely candidate for heterogeneous ice formation is soot. A large fraction of these combustion aerosols must be activated (e.g., by acquiring a liquid coating) and freeze heterogeneously. Under water-supersaturated conditions, homogeneous freezing becomes competitive. Background aerosols are not expected to play an important role in contrail formation.

• Only ~1/5 of the surface of a pure carbon particle (Graphon) can be wetted by adsorption of water, pointing toward the need for chemical processing and/or transformation of nucleation-related surface features of the soot particles.

• Our laboratory experiments suggest that even OH-treated carbon surfaces do not show good compatibilities with H_2SO_4/H_2O droplets, although the chemical processing with OH rendered the surfaces slightly more hydrophilic. Freezing of SAT is found to be completely negligible under plume conditions.

• Classical heterogeneous nucleation theory fails to give an explanation of how the soot aerosols acquire full or partial liquid coatings for jet fuel sulfur contents below ~0.2 g S per kg fuel, suggesting that processes are at work that are not considered by the standard approach (like activation after adsorption).

• Assuming the soot particles to be coated by a supercooled liquid solution, heterogeneous freezing theory predicts sufficiently rapid ice germ formation in diluted H_2SO_4 solutions for contact angles below 60°. Above water saturation, the coating may grow by condensation and this liquid phase may become visible prior to freezing.

In view of the potential importance of these processes regarding possible modifications of natural aerosols and their implications for ice nucleation, cloud formation, and subsequent heterogeneous chemical reactions in the upper troposphere and lower stratosphere, there is a strong need for more detailed measurements of particle characteristics and chemical composition in jet aircraft plumes. Certainly, aircraft-related laboratory and field measurements are required to acquire knowledge on both, possible soot activation pathways in the presence of sulfur and other trace gases, and on the capability of soot particles to act as ice forming nuclei under plume conditions. Such measurements

might lead to important implications for the far-field behavior of aging combustion aerosols and could support future modeling work, which currently has to rely on classical nucleation theory with its well-known deficiencies. In addition, numerical modeling of the competitive aerosol interaction processes in aircraft plumes is needed to investigate the physico chemical composition of contrails, to study their sensitivity on ambient conditions, and to support the interpretation of particle measurements.

REFERENCES

Appleman, H., 1953: The formation of exhaust contrails by jet aircraft. *Bull. Amer. Meteor. Soc.,* **34,** 14–20.

Baumgardner, D., and W. A. Cooper, 1994: Airborne measurements in jet contrails: Characterization of the microphysical properties of aircraft wakes and exhausts. Tech. Rep. DLR-Mitt. 94-06, 496 pp. [Available from Deutsche Forschungsanstalt für Luft-und Raumfahrt, Köln, Germany.]

Blake, D. F., and K. Kato, 1995: Latitudinal distribution of black carbon soot in the upper troposphere and lower stratosphere. *J. Geophys. Res.,* **100,** 7195–7202.

Busen, R., and U. Schumann, 1995: Visible contrail formation from fuels with different sulfur contents. *Geophys. Res. Lett.,* **22,** 1357–1360.

Cofer, W. R., D. R. Schryer, and R. S. Rogowski, 1980: The enhanced oxidation of SO_2 by NO_2 on carbon particulates. *Atmos. Environ.,* **14,** 571–575.

de Boer, J. H., 1968: *The Dynamical Character of Adsorption.* Clarendon Press, 240 pp.

DeMott, P. J., 1990: An exploratory study of ice nucleation by soot aerosols. *J. Appl. Meteor.,* **29,** 1072–1079.

Fletcher, N. H., 1969: Active sites and ice crystal nucleation. *J. Atmos. Sci.,* **26,** 1266–1271.

Fuchs, N. A., 1964: *The Mechanics of Aerosols.* Pergamon Press, 408 pp.

Gayet, J. F., G. Febvre, G. Brogniez, H. Chepfer, W. Renger, and P. Wendling, 1996: Microphysical and optical properties of cirrus and contrails: Cloud field study on 13 October 1989. *J. Atmos. Sci.,* **53,** 126–138.

Goldberg, E. D., 1985: *Black Carbon in the Environment.* Wiley-Interscience, 198 pp.

Gorbunov, B. Z., and N. A. Kakutkina, 1982: Ice crystal formation on aerosol particles with a non-uniform surface. *J. Aerosol Sci.,* **13,** 21–28.

Hagen, D. E., M. B. Trueblood, and J. Podzimek, 1991: Combustion aerosol scavenging. *Atmos. Environ.,* **25A,** 2581–2586.

——, ——, and P. D. Whitefield, 1992: A field sampling of jet exhaust aerosols. *Part. Sci. Technol.,* **10,** 53–63.

——, P. D. Whitefield, and M. B. Trueblood, 1994: Particulate characterization in the near field of commercial transport aircraft exhaust plumes using UMR-MASS. Tech. Rep. DLR-Mitt. 94-06, 496 pp. [Available from Deutsche Forschungsanstalt für Luft-und Raumfahrt, Köln, Germany.]

Hallett, J., and R. G. Oraltay, 1988: Soot particle scavenging by growing ice crystals. *Atmospheric Aerosols and Nucleation,* P. E. Wagner and G. Vali, Eds., Springer-Verlag, 303–304.

——, J. G. Hudson, and C. F. Rogers, 1989: Characterization of combustion aerosols for haze and cloud formation. *Aerosol Sci. Technol.,* **10,** 63–69.

Hamill, P., R. P. Turco, C. S. Kiang, O. B. Toon, and R. C. Whitten, 1982: An analysis of various nucleation mechanisms for sulfate particles in the stratosphere. *J. Aerosol Sci.,* **13,** 561–585.

Hofmann, D. J., and J. M. Rosen, 1978: Balloon observations of a particle layer injected by stratospheric aircraft at 23 km. *Geophys. Res. Lett.,* **5,** 511–514.

Jensen, E. J., and O. B. Toon, 1994: Ice nucleation in the upper troposphere: Sensitivity to aerosol number density, temperature, and cooling rate. *Geophys. Res. Lett.,* **21,** 2019–2022.

——, ——, and P. Hamill, 1991: Homogeneous freezing nucleation of stratospheric solution droplets. *Geophys. Res. Lett.,* **18,** 1857–1860.

Kärcher, B., 1994: A model for the transport of aircraft exhaust products in the near trail of a jet engine under atmospheric conditions: Implications for ice nucleation on soot particles. Tech. Rep. DLR-Mitt. 94-06, 496 pp. [Available from Deutsche Forschungsanstalt für Luft-und Raumfahrt, Köln, Germany.]

——, 1995: A trajectory box model for aircraft exhaust plumes. *J. Geophys. Res.,* **100,** 18 835–18 844.

——, and Th. Peter, 1995: Impact of aircraft emissions on stratospheric ozone: A research strategy. *Phys. Chem. Earth,* **20,** 123–131.

——, ——, and R. Ottmann, 1995: Contrail formation: Homogeneous nucleation of H_2SO_4/H_2O droplets. *Geophys. Res. Lett.,* **22,** 1501–1504.

——, M. M. Hirschberg, and P. Fabian, 1996: Small-scale chemical evolution of aircraft exhaust species at cruising altitudes. *J. Geophys. Res.,* **101,** 15 169–15 190.

Koop, T., U. M. Biermann, W. Raber, B. P. Luo, P. J. Crutzen, and Th. Peter, 1995: Do stratospheric aerosol droplets freeze above the ice frost point? *Geophys. Res. Lett.,* **22,** 917–920.

Luo, B. P., Th. Peter, and P. J. Crutzen, 1994: Freezing of stratospheric aerosol droplets. *Geophys. Res. Lett.,* **21,** 1447–1450.

——, K. S. Carslaw, T. Peter, and S. L. Clegg, 1995: Vapour pressures of $H_2SO_4/HNO_3/HCl/HBr/H_2O$ solutions to low stratospheric temperatures. *Geophys. Res. Lett.,* **22,** 247–250.

Miake-Lye, R. C., R. C. Brown, M. R. Anderson, and C. E. Kolb, 1994: Calculations of condensation and chemistry in an aircraft contrail. Tech. Rep. DLR-Mitt. 94-06, 496 pp. [Available from Deutsche Forschungsanstalt für Luft-und Raumfahrt, Köln, Germany.]

Middleton, P., C. S. Kiang, and V. A. Mohnen, 1982: The relative importance of various urban sulfate aerosol production mechanisms—A theoretical comparison. *Heterogeneous Atmospheric Chemistry, Geophys. Monogr.* No. 26, Amer. Geophys. Union, 221–230.

Millard, B., E. G. Caswell, E. E. Leger, and D. R. Mills, 1955: The adsorption and heats of adsorption of water on Spheron 6 and Graphon. *J. Phys. Chem.,* **59,** 976–978.

Parungo, F., B. Kopcewicz, C. Nagamoto, R. Schnell, P. Sheridan, C. Zhu, and J. Harris, 1992: Aerosol particles in the Kuwait oil fire plumes: Their morphology, size distribution, chemical composition, transport, and potential effects on climate. *J. Geophys. Res.,* **97,** 15 867–15 882.

Pitchford, M., J. G. Hudson, and J. Hallet, 1991: Size and critical supersaturation for condensation of jet engine exhaust particles. *J. Geophys. Res.,* **96,** 20 787–20 793.

Pruppacher, H. R., 1995: A new look on homogeneous ice nucleation in supercooled water drops. *J. Atmos. Sci.,* **52,** 1924–1933.

——, and J. D. Klett, 1978: *Microphysics of Clouds and Precipitation,* D. Reidel, 714 pp.

Pueschel, R. F., D. F. Blake, K. G. Snetsinger, A. D. A. Hansen, S. Verma, and K. Kato, 1992: Black carbon (soot) aerosol in the lower stratosphere and upper troposphere. *Geophys. Res. Lett.,* **19,** 1659–1662.

——, J. M. Livingston, G. V. Ferry, and T. E. DeFelice, 1994: Aerosol abundances and optical characteristics in the pacific basin free troposphere. *Atmos. Environ.,* **28,** 951–960.

Pyle, J., and Coauthors, 1994: An overview of the EASOE campaign. *Geophys. Res. Lett.,* **21,** 1191–1194.

Reiner, T., and F. Arnold, 1993: Laboratory flow reactor measurements of the reaction $SO_3 + H_2O + M \rightarrow H_2SO_4 + M$: Implications for gaseous H_2SO_4 and aerosol formation in the plumes of jet aircraft. *Geophys. Res. Lett.,* **20,** 2659–2662.

Rosen, J. M., and R. Greegor, 1974: Jet engine soot emission measured at altitude. *J. Aircr.,* **11,** 243–245.

Schryer, D. R., W. R. Cofer, and R. S. Rogowski, 1980: Synergistic effects in trace gas–aerosol interactions. *Science,* **209,** 723.

Schumann, U., 1994: On the effect of emissions from aircraft engines on the state of the atmosphere. *Ann. Geophys.,* **12,** 365–384.

——, 1996: On conditions for contrail formation from aircraft exhausts. *Meteor. Z.,* **5,** 4–23.

——, J. Ström, R. Busen, R. Baumann, K. Gierens, M. Krautstrunk, F. Schröder, and J. Stingl, 1996: In situ observations of particles in jet aircraft exhausts and contrails for different sulfur containing fuels. *J. Geophys. Res.,* **101,** 6853–6869.

Sedunov, Y. S., 1974: *Physics of Drop Formation in the Atmosphere,* John Wiley, 234 pp.

Stolarski, R. S., and H. L. Wesoky, 1993: The atmospheric effects of stratospheric aircraft: A third program report. NASA Ref. Publ. RP-1313, 413 pp. [Available from NASA/Langley Research Center, Hampton, VA 23681-0001.]

——, and ——, 1995: The atmospheric effects of stratospheric aircraft: A fourth program report. NASA Ref. Publ. RP-1359, 236 pp. [Available from NASA, Code JTT, Washington, DC 20546–0001.]

Talbot, R., A. Vijgen, and R. Harris, 1992: Soluble species in the arctic summer troposphere: Acidic gases, aerosols, and precipitation. *J. Geophys. Res.,* **97,** 531–543.

Thlibi, J., and J. C. Petit, 1994: A study of the NO_y/soot interaction in the temperature range 303–1223 K. Tech. Rep. DLR-Mitt. 94-06, 496 pp. [Available from Deutsche Forschungsanstalt für Luft-und Raumfahrt, Köln, Germany.]

Wagner, H. G., 1978: Soot formation in combustion. *17th Symp. on Combustion,* Pittsburgh, PA, The Combustion Institute, 3–19.

Warren, S. G., 1984: Optical constants of ice from the ultraviolet to the microwave. *Appl. Opt.,* **23,** 1206–1225.

Whitefield, P. D., M. B. Trueblood, and D. E. Hagen, 1993: Size and hydration characteristics of laboratory simulated jet engine combustion aerosols. *Part. Sci. Technol.,* **11,** 25–36.

Wyslouzil, B. E., K. L. Carleton, D. M. Sonnenfroh, and W. T. Rawlins, 1994: Observation of hydration of single, modified carbon aerosols. *Geophys. Res. Lett.,* **21,** 2107–2110.

Young, G. J., J. J. Chessick, F. H. Healey, and A. C. Zettlemoyer, 1954: Thermodynamics of the adsorption of water on Graphon from heats of immersion and adsorption data. *J. Phys. Chem.,* **58,** 313–315.

Zhao, J., and R. P. Turco, 1995: Nucleation simulations in the wake of a jet aircraft in stratospheric flight. *J. Aerosol Sci.,* **26,** 779–795.